UC Berkeley
UC Berkeley Previously Published Works

Title

Creation of skyrmions in van der Waals ferromagnet Fe3GeTe2 on (Co/Pd)n superlattice

Permalink

https://escholarship.org/uc/item/3ft8f93d

Journal

Science Advances, 6(36)

ISSN

2375-2548

Authors

Yang, M
Li, Q
Chopdekar, RV
et al.

Publication Date

2020-09-04

DOI

10.1126/sciadv.abb5157

Peer reviewed

CONDENSED MATTER PHYSICS

Creation of skyrmions in van der Waals ferromagnet Fe₃GeTe₂ on (Co/Pd)ₙ superlattice

M. Yang[1]*, Q. Li[1]*†, R. V. Chopdekar[2], R. Dhall[3], J. Turner[3], J. D. Carlström[1], C. Ophus[3], C. Klewe[2], P. Shafer[2], A. T. N'Diaye[2], J. W. Choi[4], G. Chen[5], Y. Z. Wu[6], C. Hwang[7], F. Wang[1], Z. Q. Qiu[1]†

Magnetic skyrmions are topological spin textures, which usually exist in noncentrosymmetric materials where the crystal inversion symmetry breaking generates the so-called Dzyaloshinskii-Moriya interaction. This requirement unfortunately excludes many important magnetic material classes, including the recently found two-dimensional van der Waals (vdW) magnetic materials, which offer unprecedented opportunities for spintronic technology. Using photoemission electron microscopy and Lorentz transmission electron microscopy, we investigated and stabilized Néel-type magnetic skyrmion in vdW ferromagnetic Fe₃GeTe₂ on top of (Co/Pd)ₙ in which the Fe₃GeTe₂ has a centrosymmetric crystal structure. We demonstrate that the magnetic coupling between the Fe₃GeTe₂ and the (Co/Pd)ₙ could create skyrmions in Fe₃GeTe₂ without the need of an external magnetic field. Our results open exciting opportunities in spintronic research and the engineering of topologically protected nanoscale features by expanding the group of skyrmion host materials to include these previously unknown vdW magnets.

INTRODUCTION

It was found recently that van der Waals (vdW) magnetic materials (1, 2) exhibit many fascinating properties such as the giant tunneling magnetoresistance (3), unconventional responses from quantum metamaterials (4), the pressure (5, 6) and electrical (7, 8) control of magnetism, etc. However, the crystal structures of most vdW magnetic materials (9) have inversion symmetry, thus nominally disqualifying the generation of the so-called Dzyaloshinskii-Moriya interactions (DMIs) (10, 11). The recent success in expanding skyrmion materials from noncentrosymmetric magnets (12–14) to centrosymmetric magnets (15, 16) by dipole-dipole interaction makes it promising to search for skyrmions in vdW magnetic materials by magnetic interaction.

Among the vdW magnetic materials, Fe₃GeTe₂ (FGT) is an itinerant vdW ferromagnet with a relatively high Curie temperature ($T_C \sim 230$ K) and many interesting magnetic properties (17–20). In particular, the tunable T_C and the perpendicular magnetic stripe domains (21–24) in FGT make it an ideal candidate for the formation of magnetic skyrmions. Despite the various theoretical proposals (25–27), skyrmions have only been observed in vdW magnets within an out-of-plane magnetic field so far (28–32). However, the results are very controversial and confusing on the skyrmion structure [Bloch type (28, 29) or Néel type (30–32)], raising the question on the physical origin of the skyrmion formation within the magnetic field (inherent material properties or due to the presence of the magnetic field). To explore the underlying mechanism, it is very important to realize skyrmions in magnetic vdW materials as the ground state in the absence of magnetic field. Here, in this work, we demonstrate a realization of Néel-type magnetic skyrmions in FGT in the heterostructures of

FGT/[Co/Pd]₁₀ multilayers at zero magnetic field, which is likely to be stabilized by the magnetic interlayer coupling.

RESULTS

We fabricated the sample of Pd(1)/FGT/Pd(wedge)/[Co(0.4)/Pd(0.9)]₁₀/ Pd(3) on a Si(111) substrate (see the "MATERIALS AND METHODS" section), where the numbers in parentheses are the film thicknesses in units of nanometer. The Pd wedge (0 to 16 nm) permits a monotonic decrease in the ferromagnetic coupling between the FGT and [Co/ Pd]₁₀ with increasing Pd spacer layer thickness (33). Figure 1A shows the schematic drawing of the FGT atomic structure: Covalently bonded Fe₃Ge layers are separated by two adjacent Te layers that are vdW gapped. The Fe atoms occupy two inequivalent Wyckoff sites denoted as Fe1 and Fe2: The Fe1 atoms form a hexagonal net, and the Fe2 atoms are bonded covalently with the Ge atoms to form a hexagonal structure of $P6_3/mmc$ space group. High-resolution scanning transmission electron microscopy (TEM) image together with sharp electron diffraction patterns indicate the high quality of our single crystalline FGT samples (Fig. 1B). There is no evidence of inversion symmetry breaking from the TEM result of the bulk FGT crystal. X-ray magnetic circular dichroism (XMCD) manifests as the difference of x-ray absorption spectra for magnetization parallel and antiparallel to the x-ray incidence direction (Fig. 1, C and E). Then, element-resolved Co and Fe XMCD measurements were performed by tuning the x-ray photon energy across the Co L_3 edge absorption energy of 778.0 eV (Fig. 1C) and the Fe L_3 edge absorption energy of 706.3 eV (Fig. 1E), respectively. Since XMCD measures the projection of the magnetization along the x-ray incidence direction, we obtained the out-of-plane and in-plane hysteresis loops at normal ($\theta = 90°$) and grazing ($\theta = 20°$) incidence of the circularly polarized x-rays (Fig. 1D), respectively. The Co/Pd multilayers exhibit an out-of-plane easy-axis hysteresis loop and an in-plane hard-axis hysteresis loop (Fig. 1D), consistent with the perpendicular magnetic anisotropy of Co/Pd multilayers in this thickness range (34, 35). The FGT hysteresis loops also exhibit a much smaller saturation field of the out-of-plane hysteresis loop than that of the in-plane hysteresis loop (Fig. 1F), showing an out-of-plane easy magnetization

¹Department of Physics, University of California, Berkeley, CA 94720, USA. ²Advanced Light Source, Lawrence Berkeley National Laboratory, Berkeley, CA 94720, USA. ³Molecular Foundry, Lawrence Berkeley National Laboratory, Berkeley, CA 94720, USA. ⁴Center for Spintronics, Korea Institute of Science and Technology, Seoul 02792, Republic of Korea. ⁵Department of Physics, University of California, Davis, CA 95616, USA. ⁶Department of Physics and State Key Laboratory of Surface Physics, Fudan University, Shanghai 200433, China. ⁷Korea Research Institute of Standards and Science, Yuseong, Daejeon 305-340, Republic of Korea.
*These authors contributed equally to this work.
†Corresponding author. Email: qianli2015@berkeley.edu (Q.L.); qiu@berkeley.edu (Z.Q.Q.)
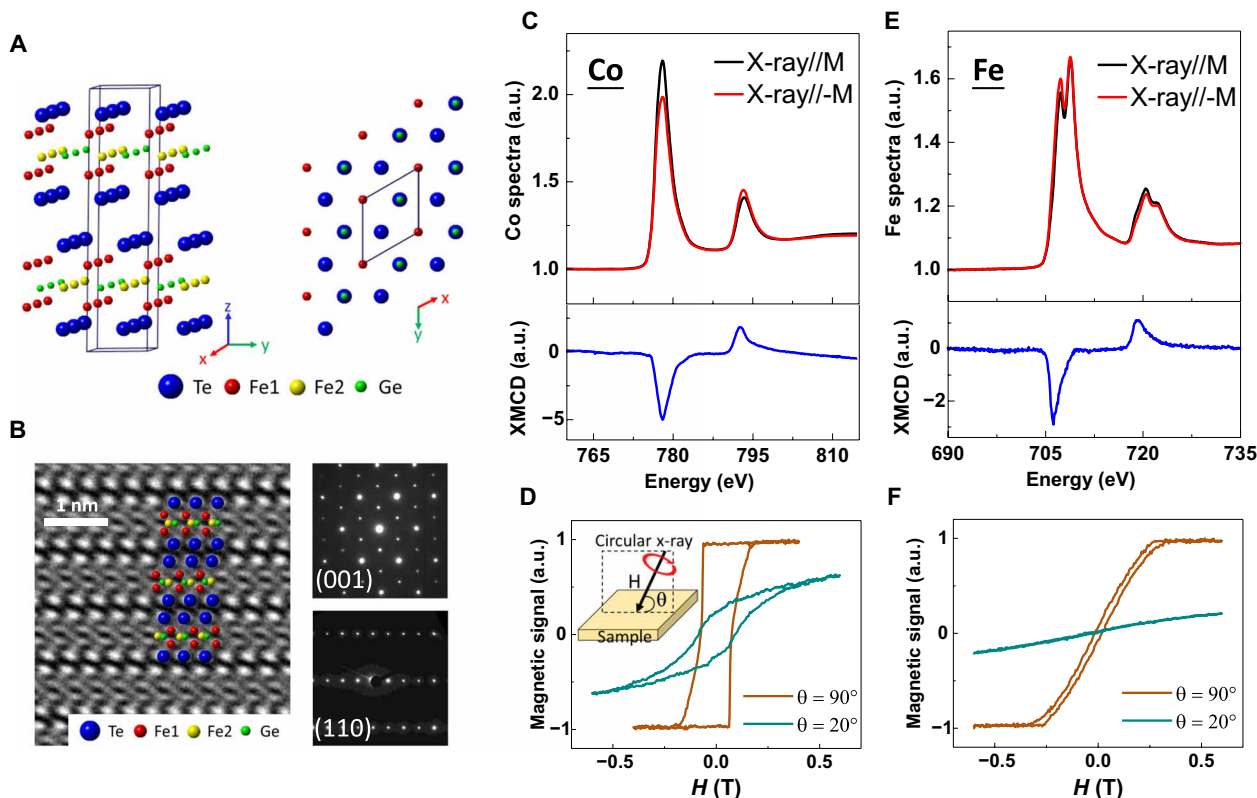
Fig. 1. Crystal structure and element-resolved XMCD measurement. (**A**) Atomic structure of FGT. (**B**) High-resolution cross-section scanning TEM image (left) and the corresponding electron diffraction patterns of (001)-oriented (top right) and (110)-oriented (bottom right) FGT. There is no evidence of inversion symmetry breaking in the bulk FGT crystal. Element-resolved XMCD measurements from (**C**) the Co absorption edge and (**E**) the Fe absorption edge, respectively. a.u., arbitrary units. Both (**D**) the Co and (**F**) the Fe hysteresis loops show an out-of-plane easy magnetization axis from Co/Pd multilayers and FGT vdW material. The inset in (D) is the schematic drawing for the hysteresis loop measurement, where θ is the angle between the x-ray incidence direction and the sample surface.

axis. The zero remanence is consistent with the formation of the stripe domain (labyrinthine domain) phase in FGT (*22, 24*). All the XMCD measurements were performed at $T = 110$ K, well below the bulk FGT Curie temperature.

The sample was magnetized along the out-of-plane direction (+z direction) at room temperature to force the Co/Pd multilayers into a single domain (see fig. S1) and then imaged at zero field using photoemission electron microscopy (PEEM) at $T = 110$ K along the Pd wedge to enable a systematic study of the FGT domain pattern as a function of the Pd thickness. As a reference, FGT domains on top of a thick Pd layer ($d_{Pd} = 16$ nm) are shown in Fig. 2B to represent the zero-coupling case. As expected, we observed the same stripe domains as in the free FGT flake (*22*) with equal amounts of bright and dark stripes whose magnetizations are in the +z and −z directions, respectively. As the Pd spacer thickness decreases to 5 nm to turn on the magnetic coupling between the FGT and [Co/Pd]$_{10}$, some of the dark stripes (whose magnetization is in −z direction and antiparallel to the [Co/Pd]$_{10}$ magnetization direction) break into bubbles (later shown in Fig. 3 to be Néel-type skyrmions). With further increase in the coupling by reducing the Pd thickness to 1.5 nm, more dark stripes break into bubbles (skyrmions). Note that the stripe width (~160 nm) and the bubble diameter (~140 nm) are more or less unchanged with increasing interlayer coupling strength. Since the magnetic domains of FGT has been confirmed, not vary from flake to flake in the thick region above 50 nm (*22*), the

slight change of FGT minority domain width in different flakes may be due to different thicknesses of Pd spacer layer. We also quantitatively analyzed the PEEM images in Fig. 2B to obtain the bubble area and the normalized magnetization (the areal difference between the bright and dark domains). The results clearly show that as the interlayer coupling increases by reducing the Pd spacer layer thickness from 16 to 1.5 nm, the magnetization increases (Fig. 2E) at the expense of reducing the area (Fig. 2E) of minority domains (dark stripes). The bubble area simultaneously increases, further confirming our observation that the bubbles (skyrmions) are formed by breaking the dark stripes (antiparallel to the [Co/Pd]$_{10}$ magnetization) into bubbles. Note that our result does not depend on the mechanism of the interlayer coupling mechanism but only on the existence of this coupling. In addition, since the [Co/Pd]$_{10}$ is at the single domain state in Fig. 2B, stray field effect should be negligible as compared to the interlayer coupling (*33*).

We then demagnetized the sample to change the [Co/Pd]$_{10}$ from a single-domain magnetized state (+z direction) into multidomains. Element-resolved PEEM measurements provide both the [Co/Pd]$_{10}$ and FGT domain images by tuning the x-ray photon energy to the Co L_3 edge or Fe L_3 edge absorption energies, respectively. The [Co/Pd]$_{10}$ multilayers exhibit a dendrite-like multidomain pattern with alternating up (+z direction, bright area) and down (−z direction, dark area) magnetizations (domains surrounding the center FGT flake in Fig. 2C). Consequently, we observed both dark and bright
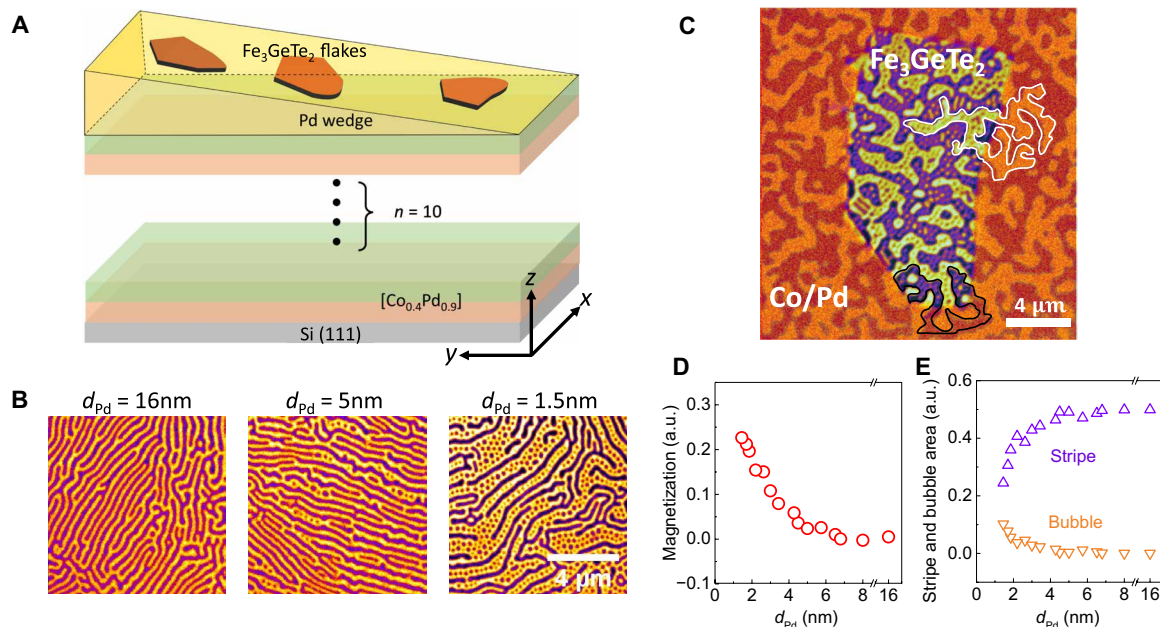
Fig. 2. Creating magnetic skyrmions in FGT by the magnetic interlayer coupling between FGT and [Co/Pd]$_{10}$ multilayers. (**A**) Schematic drawing of the sample structure, where the wedged Pd spacer layer tunes the coupling strength between FGT and perpendicularly magnetized [Co/Pd]$_{10}$ multilayers. (**B**) PEEM images of the FGT magnetic domains at three different thicknesses of the Pd spacer layer. The bright and dark contrasts correspond to an out-of-plane magnetization in the +z and −z directions, respectively. The [Co/Pd]$_{10}$ underlayer was magnetized in the +z direction. Dark stripes are gradually broken into bubbles (skyrmions) as the coupling strength increases by decreasing the Pd thickness. The thicknesses of FGT flakes are 130, 150, and 130 nm, respectively. (**C**) Magnetic domain images of the FGT obtained at Fe L_3 edge (the center flake) and the [Co/Pd]$_{10}$ obtained at Co L_3 edge (surrounding area) at d_{Pd} = 0.9 nm after demagnetizing the [Co/Pd]$_{10}$ into multidomains. The magnetization direction inside the bubbles is always antiparallel to the underlayer [Co/Pd]$_{10}$ magnetization. (**D**) FGT normalized magnetization calculated from the areal difference between the bright and the dark domains of the PEEM images and (**E**) from areal fractions of stripes and bubbles (antiparallel to [Co/Pd]$_{10}$ magnetization) as a function of Pd spacer layer thickness.

bubbles grouped into dendrite-like domains in the FGT flake. It should be mentioned that PEEM only measures the top layer magnetization due to the finite escape depth of photoemission electrons (a few nanometers). However, since the bright (or dark) [Co/Pd]$_{10}$ domain connects well with bright (or dark) FGT dendrite-like domains at the boundary of the FGT flake (see white and dark dendrite-like profiles in Fig. 2C), it can be clearly seen that the bubble magnetization in FGT is always antiparallel to the [Co/Pd]$_{10}$ underlayer local magnetization direction, the same as in Fig. 2B when the [Co/Pd]$_{10}$ underlayer is in a single domain state. Therefore, we conclude that the transition of the stripe phase to skyrmion (bubble) phase in FGT must be a result of its magnetic coupling to the perpendicularly magnetized [Co/Pd]$_{10}$.

To probe the topological structure of the observed bubbles (*36*), we used Lorentz TEM (LTEM) to resolve the magnetic structure of the domain wall. By defocusing the imaging lens, the Lorentz deflection of the electron beam due to a local in-plane magnetic field will diverge or converge to generate intensity contrast from these regions of the sample. Note that the PEEM experiment could not reveal the strong coupling limit for d_{Pd} < 1 nm (in this limit, all minority stripes in Fig. 2 should be converted into bubbles) due to the oxidization of Co layer. Thus, we prepared a sample of [Co/Pd]$_{10}$/FGT on a Si$_3$N$_4$ membrane (see the "MATERIALS AND METHODS" section) by growing [Co/Pd]$_{10}$ on top of FGT without the Pd spacer layer between FGT and [Co/Pd]$_{10}$, which corresponds to the d_{Pd} = 0 nm case for sample structure used for PEEM measurements (Fig. 2). [Co/Pd]$_{10}$ was magnetized along the out-of-plane direction at room temperature into a single

domain state, so any magnetic contrast in LTEM images comes from the in-plane component of magnetization in the FGT layer. Figure 3A shows the schematic drawing of the sample side view and TEM image of the top view. A well-established method for the detection of the spin configuration of a skyrmion is to compare the defocused LTEM images at various tilting angles of the sample relative to the electron beam (*37, 38*). Since the contrast in LTEM arises from the projection of the magnetization curl along the beam propagation direction, a Néel-type skyrmion should not show any contrast at normal incidence but show opposite contrasts in each halves of the skyrmion after tilting the sample (*37*). We found that the system has Néel-type skyrmions at zero field (Fig. 3B) whose LTEM image exhibits zero contrast at normal incidence (Fig. 3C, middle), dark/bright contrasts within two halves of the skyrmion after tilting the sample by +30° (Fig. 3C, left), and a contrast reversal after tilting the sample in the opposite direction (i.e., −30°; Fig. 3C, right). The line profile in Fig. 3C more clearly shows the contrast reversal (Fig. 3D) for opposite tilting angles, further confirming the Néel-type structure of the skyrmion. To construct the magnetization distribution map, we analyzed a series of LTEM images (see fig. S2) from underfocus to overfocus using the exit wave phase reconstruction method (*39*). Figure 3E shows the magnetization distribution of the Néel-type skyrmions, where hedgehog-like spin configurations were observed. It should be mentioned that the LTEM images in Fig. 3 were obtained in zero magnetic field so that any field effect on the wall type of skyrmions was eliminated. In another word, the Néel-type structure of the skyrmion should be an inherent property of FGT.
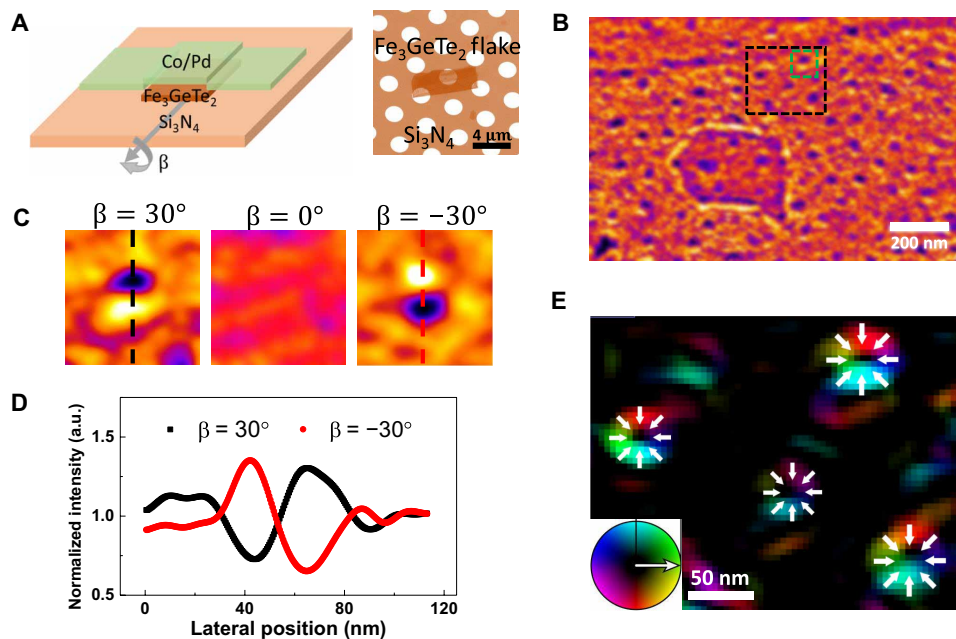
Fig. 3. Néel-type skyrmions observed by LTEM in the system of FGT/[Co/Pd]$_{10}$ multilayers. (A) Schematic drawing of sample structure and TEM image of FGT flake on a porous Si$_3$N$_4$ membrane. The thickness of FGT flake here is 70 nm. **(B)** LTEM images of FGT/[Co/Pd]$_{10}$ at a sample tilting angle of 30°. **(C)** LTEM images taken from selected area in (B) (green dashed box) at sample tilting angles of 30°, 0°, and − 30°. The zero contrast at 0° tilting angle and the reversed contrasts at opposite tilting angles indicate the Néel-type structure of the skyrmion. All LTEM measurements were performed at liquid nitrogen temperature. **(D)** Line profiles of the contrast from the same skyrmion at opposite tilting angles, showing the contrast reversal of the Néel-type skyrmion at opposite tilting angles. **(E)** The magnetization distribution obtained by exit wave phase reconstruction of the selected LTEM data [black dashed box in (B)]. The white arrows and the color wheel indicate the in-plane direction of the magnetization.

DISCUSSION

As shown in our previous work (22), the stripe domains in FGT are a result of the competition among the exchange interaction, magnetic anisotropy, and dipolar interaction. In the limit of the strong dipolar interaction such as in bulk FGT, the stripe width reaches a minimum width (on the order of 10^2 nm). This is the stripe phase in the d_{Pd} = 16-nm sample (Fig. 2B), where the 16-nm Pd is thick enough to decouple the coupling between FGT and [Co/Pd]$_{10}$. It is very important to point out that the stripe phase retains the up/down symmetry (inversion symmetry along the z axis), e.g., the magnetic stripe pattern (both the up/down area ratio and the shape) is invariant after changing S_z to $-S_z$, where S_z is the spin component of FGT along the surface normal direction. In contrast, the skyrmion phase breaks the up/down symmetry in the sense that both the up/down domain areas and the up/down domain shapes (e.g., separated bubbles versus connected area) will change after changing S_z to $-S_z$. Therefore, the existence of stripe domains in the d_{Pd} = 16-nm sample shows that inversion symmetry breaking along the z axis at the FGT/Pd interface or any possible sample surface oxidization is certainly not strong enough to stabilize magnetic skyrmions in FGT. Therefore, it must be the magnetic coupling between the stripe phase and the perpendicular magnetization of the [Co/Pd]$_{10}$ that drives and stabilizes the skyrmion phase in FGT in the d_{Pd} = 5 and 1.5 nm samples (Fig. 2B).

We can qualitatively understand the transition from the stripe phase to the skyrmion phase from the following scenario. The coupling between FGT and [Co/Pd]$_{10}$ should result in a net perpendicular magnetization in FGT by reducing the minority domain area (dark stripes in Fig. 2B). Since the stripes are already reaching the minimum width, the minority stripes have to be broken into segments (equivalent bubbles) to reduce their relative area. Consequently, as the magnetiza-

tion increases with the coupling strength, more and more bubbles appear by breaking the minority stripes as shown in Fig. 2, B, D, and E. Our result may also explain the existence of skyrmions within an out-of-plane magnetic field where the field also reduces the minority domains. However, since LTEM measurement can only have magnetic field applied along the electron beam direction, there is an inevitable in-plane component of magnetic field when imaging the Néel-type skyrmions at a tilting angle of the sample. It is not clear at present on how this in-plane component of magnetic field affects the skyrmion formation. Using LTEM, we analyzed the stripe domains in a FGT flake without the [Co/Pd]$_{10}$ and identified the Néel-type walls of the stripes (see fig. S3). Since there is no broken inversion symmetry in FGT crystal, it is unclear if the observed Néel-type wall is from mechanisms other than DMI [e.g., dipole-dipole interaction (15, 16)]. We would like to leave this topic as an open question for future studies. In summary, we demonstrate the realization of magnetic skyrmions in magnetic vdW FGT by magnetic coupling between FGT and out-of-plane magnetized Co/Pd multilayers. Our findings provide an effective method to induce magnetic skyrmions in vdW magnets at zero magnetic field in magnetic heterostructures, opening a new avenue to vdW magnet-based topological spintronics such as the zero-field skyrmion motion in vdW ferromagnets. The expansion of skyrmion materials to the vdW materials by this work should generate new opportunities for both magnetic research and vdW material research.

MATERIALS AND METHODS
Sample fabrication
The sample of Pd wedge (0 to 16 nm)/[Co$_{0.4}$/Pd$_{0.9}$]$_{10}$/Pd (3) on a Si(111) substrate was grown by molecular beam epitaxy in an ultrahigh

vacuum chamber with a base pressure of 5×10^{-10} torr. All films were grown at room temperature from the thermal crucibles. The Si(111) substrate was first annealed to ~200°C. Then, a 3-nm thick bottom Pd layer was grown as a seed layer. The thicknesses of Co and Pd in the stack structure were chosen to exhibit strong out-of-plane magnetic anisotropy. Then, a Pd wedge (0 to 16 nm) was grown by moving the substrate behind a knife-edge shutter during the growth. FGT flakes were exfoliated from a high-quality bulk FGT single crystal, which was fabricated by chemical vapor transport method. To facilitate the FGT exfoliation, the sample was heated to 50°C, exfoliated, and transferred immediately (within 15 min) into the ultrahigh vacuum chamber. Last, a 1.0-nm-thick Pd protection layer was grown on top of the sample from a thermal crucible.

Samples on membranes were prepared for LTEM imaging. A porous TEM grid with a 200-nm Si$_3$N$_4$ film and 2.0-µm-diameter pores window was used as substrate. FGT flakes were exfoliated onto a polydimethylsiloxane (PDMS) stamp attached to a glass slide. The glass slide was subsequently attached to a micromanipulator with a microscope to align the exfoliated flakes with the substrate. The flakes were transferred by bringing the PDMS stamp into contact with the substrate and slowly peeling it off, all at room temperature. After transferring the flakes, the sample was transferred into the ultrahigh vacuum chamber. In the chamber, the sample was first annealed at ~100°C, after which 10 stacks of Co/Pd multilayer were deposited.

XMCD, PEEM, and LTEM measurement

XMCD measurements were performed at Beamline 4.0.2 and 6.3.1 of the Advanced Light Source by switching the magnetization parallel and antiparallel to the propagation direction of a circularly polarized x-rays at normal incidence. Magnetic domain images from PEEM were taken at Beamline 11.0.1 of the Advanced Light Source using left- and right-circular polarized x-rays at a photon energy of 706.3 eV (778.0 eV), which corresponds to the energy of maximum XMCD at Fe (Co) L_3 edge.

The LTEM images were acquired using the FEI Themis TEM in molecular foundry. A series of images were obtained in Lorentz mode with various defocus values from −400 to 400 µm at a step of 100 µm. A Gerchberg-Saxton algorithm was used for the exit wave phase reconstruction, in combination with an iterative algorithm to remove the in-plane imaging distortions.

SUPPLEMENTARY MATERIALS

Supplementary material for this article is available at http://advances.sciencemag.org/cgi/content/full/6/36/eabb5157/DC1

REFERENCES AND NOTES

1. C. Gong, L. Li, Z. Li, H. Ji, A. Stern, Y. Xia, T. Cao, W. Bao, C. Wang, Y. Wang, Z. Q. Qiu, R. J. Cava, S. G. Louie, J. Xia, X. Zhang, Discovery of intrinsic ferromagnetism in two-dimensional van der Waals crystals. *Nature* **546**, 265–269 (2017).
2. B. Huang, G. Clark, E. Navarro-Moratalla, D. R. Klein, R. Cheng, K. L. Seyler, D. Zhong, E. Schmidgall, M. A. McGuire, D. H. Cobden, W. Yao, D. Xiao, P. Jarillo-Herrero, X. Xu, Layer-dependent ferromagnetism in a van der Waals crystal down to the monolayer limit. *Nature* **546**, 270–273 (2017).
3. T. Song, X. Cai, M. W.-Y. Tu, X. Zhang, B. Huang, N. P. Wilson, K. L. Seyler, L. Zhu, T. Taniguchi, K. Watanabe, M. A. McGuire, D. H. Cobden, D. Xiao, W. Yao, X. Xu, Giant tunneling magnetoresistance in spin-filter van der Waals heterostructures. *Science* **360**, 1214–1218 (2018).
4. J. C. W. Song, N. M. Gabor, Electron quantum metamaterials in van der Waals heterostructures. *Nat. Nanotechnol.* **13**, 986–993 (2018).
5. T. Song, Z. Fei, M. Yankowitz, Z. Lin, Q. Jiang, K. Hwangbo, Q. Zhang, B. Sun, T. Taniguchi, K. Watanabe, M. A. McGuire, D. Graf, T. Cao, J.-H. Chu, D. H. Cobden, C. R. Dean, D. Xiao, X. Xu, Switching 2D magnetic states via pressure tuning of layer stacking. *Nat. Mater.* **18**, 1298–1302 (2019).
6. T. Li, S. Jiang, N. Sivadas, Z. Wang, Y. Xu, D. Weber, J. E. Goldberger, K. Watanabe, T. Taniguchi, C. J. Fennie, K. F. Mak, J. Shan, Pressure-controlled interlayer magnetism in atomically thin CrI$_3$. *Nat. Mater.* **18**, 1303–1308 (2019).
7. B. Huang, G. Clark, D. R. Klein, D. MacNeill, E. Navarro-Moratalla, K. L. Seyler, N. Wilson, M. A. McGuire, D. H. Cobden, D. Xiao, W. Yao, P. Jarillo-Herrero, X. Xu, Electrical control of 2D magnetism in bilayer CrI$_3$. *Nat. Nanotech.* **13**, 544–548 (2018).
8. Z. Wang, T. Zhang, M. Ding, B. Dong, Y. Li, M. Chen, X. Li, J. Huang, H. Wang, X. Zhao, Y. Li, D. Li, C. Jia, L. Sun, H. Guo, Y. Ye, D. Sun, Y. Chen, T. Yang, J. Zhang, S. Ono, Z. Han, Z. Zhang, Electric-field control of magnetism in a few-layered van der Waals ferromagnetic semiconductor. *Nat. Nanotech.* **13**, 554–559 (2018).
9. M. Gibertini, M. Koperski, A. F. Morpurgo, K. S. Novoselov, Magnetic 2D materials and heterostructures. *Nat. Nanotechnol.* **14**, 408–419 (2019).
10. I. E. Dzyaloshinskii, Thermodynamic theory of "weak" ferromagnetism in antiferromagnetic substances. *Sov. Phys. JETP* **5**, 1259–1272 (1957).
11. T. Moriya, Anisotropic superexchange interaction and weak ferromagnetism. *Phys. Rev.* **120**, 91–98 (1960).
12. S. Mühlbauer, B. Binz, F. Jonietz, C. Pfleiderer, A. Rosch, A. Neubauer, R. Georgii, P. Böni, Skyrmion lattice in a chiral magnet. *Science* **323**, 915–919 (2009).
13. X. Z. Yu, Y. Onose, N. Kanazawa, J. H. Park, J. H. Han, Y. Matsui, N. Nagaosa, Y. Tokura, Real-space observation of a two-dimensional skyrmion crystal. *Nature* **465**, 901–904 (2010).
14. I. Kézsmárki, S. Bordács, P. Milde, E. Neuber, L. M. Eng, J. S. White, H. M. Rønnow, C. D. Dewhurst, M. Mochizuki, K. Yanai, H. Nakamura, D. Ehlers, V. Tsurkan, A. Loidl, Néel-type skyrmion lattice with confined orientation in the polar magnetic semiconductor GaV$_4$S$_8$. *Nat. Mater.* **14**, 1116–1122 (2015).
15. X. Yu, M. Mostovoy, Y. Tokunaga, W. Zhang, K. Kimoto, Y. Matsui, Y. Kaneko, N. Nagaosa, Y. Tokura, Magnetic stripes and skyrmions with helicity reversals. *Proc. Natl. Acad. Sci. U.S.A.* **109**, 8856–8860 (2012).
16. X. Z. Yu, Y. Tokunaga, Y. Kaneko, W. Z. Zhang, K. Kimoto, Y. Matsui, Y. Taguchi, Y. Tokura, Biskyrmion states and their current-driven motion in a layered manganite. *Nat. Commun.* **5**, 3198 (2014).
17. Y. Zhang, H. Lu, X. Zhu, S. Tan, W. Feng, Q. Liu, W. Zhang, Q. Chen, Y. Liu, X. Luo, D. Xie, L. Luo, Z. Zhang, X. Lai, Emergence of Kondo lattice behavior in a van der Waals itinerant ferromagnet, Fe$_3$GeTe$_2$. *Sci. Adv.* **4**, eaao6791 (2018).
18. C. Tan, J. Lee, S.-G. Jung, T. Park, S. Albarakati, J. Partridge, M. R. Field, D. G. McCulloch, L. Wang, C. Lee, Hard magnetic properties in nanoflake van der Waals Fe$_3$GeTe$_2$. *Nat. Commun.* **9**, 1554 (2018).
19. M. Alghamdi, M. Lohmann, J. Li, P. R. Jothi, Q. Shao, M. Aldosary, T. Su, B. P. T. Fokwa, J. Shi, Highly efficient spin–orbit torque and switching of layered ferromagnet Fe$_3$GeTe$_2$. *Nano Lett.* **19**, 4400–4405 (2019).
20. X. Wang, J. Tang, X. Xia, C. He, J. Zhang, Y. Liu, C. Wan, C. Fang, C. Guo, W. Yang, Y. Guang, X. Zhang, H. Xu, J. Wei, M. Liao, X. Lu, J. Feng, X. Li, Y. Peng, H. Wei, R. Yang, D. Shi, X. Zhang, Z. Han, Z. Zhang, G. Zhang, G. Yu, X. Han, Current-driven magnetization switching in a van der Waals ferromagnet Fe$_3$GeTe$_2$. *Sci. Adv.* **5**, eaaw8904 (2019).
21. Y. Deng, Y. Yu, Y. Song, J. Zhang, N. Z. Wang, Z. Sun, Y. Yi, Y. Z. Wu, S. Wu, J. Zhu, J. Wang, X. H. Chen, Y. Zhang, Gate-tunable room-temperature ferromagnetism in two-dimensional Fe$_3$GeTe$_2$. *Nature* **563**, 94–99 (2018).
22. Q. Li, M. Yang, C. Gong, R. V. Chopdekar, A. T. N'Diaye, J. Turner, G. Chen, A. Scholl, P. Shafer, E. Arenholz, A. K. Schmid, S. Wang, K. Liu, N. Gao, A. S. Admasu, S.-W. Cheong, C. Hwang, J. Li, F. Wang, X. Zhang, Z. Q. Qiu, Patterning-induced ferromagnetism of Fe$_3$GeTe$_2$ van der Waals materials beyond room temperature. *Nano Lett.* **18**, 5974–5980 (2018).
23. M. Yang, Q. Li, R. V. Chopdekar, C. Stan, S. Cabrini, J. Choi, S. Wang, T. Wang, N. Gao, A. Scholl, N. Tamura, C. Hwang, F. Wang, Z. Q. Qiu, Highly enhanced curie temperature in Ga-implanted Fe$_3$GeTe$_2$ van der Waals material. *Adv. Quantum Technol.* **2**, 2000017 (2020).
24. Z. Fei, B. Huang, P. Malinowski, W. Wang, T. Song, J. Sanchez, W. Yao, D. Xiao, X. Zhu, A. F. May, W. Wu, D. H. Cobden, J.-H. Chu, X. Xu, Two-dimensional itinerant ferromagnetism in atomically thin Fe$_3$GeTe$_2$. *Nat. Mater.* **17**, 778–782 (2018).
25. Q. Tong, F. Liu, J. Xiao, W. Yao, Skyrmions in the Moiré of van der Waals 2d magnets. *Nano Lett.* **18**, 7194–7199 (2018).
26. J. Liu, M. Shi, P. Mo, J. Lu, Electrical-field-induced magnetic Skyrmion ground state in a two-dimensional chromium tri-iodide ferromagnetic monolayer. *AIP Adv.* **8**, 055316 (2018).
27. A. K. Behera, S. Chowdhury, S. R. Das, Magnetic skyrmions in atomic thin CrI$_3$ monolayer. *Appl. Phys. Lett.* **114**, 232402 (2019).
28. M.-G. Han, J. A. Garlow, Y. Liu, H. Zhang, J. Li, D. DiMarzio, M. W. Knight, C. Petrovic, D. Jariwala, Y. Zhu, Topological magnetic-spin textures in two-dimensional van der Waals Cr$_2$Ge$_2$Te$_6$. *Nano Lett.* **19**, 7859–7865 (2019).

29. B. Ding, Z. Li, G. Xu, H. Li, Z. Hou, E. Liu, X. Xi, F. Xu, Y. Yao, W. Wang, Observation of magnetic Skyrmion Bubbles in a van der Waals ferromagnet Fe3GeTe2. *Nano Lett.* **20**, 868–873 (2020).

30. T. Park, L. Peng, J. Liang, A. Hallal, X. Zhang, S. J. Kim, K. M. Song, K. Kim, M. Weigand, G. Schuetz, S. Finizio, J. Raabe, J. Xia, Y. Zhou, M. Ezawa, X. Liu, J. Chang, H. C. Koo, Y. D. Kim, M. Chshiev, A. Fert, H. Yang, X. Yu, S. Woo, Observation of magnetic skyrmion crystals in a van der Waals ferromagnet Fe3GeTe2. arXiv:1907.01425 [cond-mat.mtrl-sci] (2019).

31. Y. Wu, S. Zhang, G. Yin, J. Zhang, W. Wang, Y. L. Zhu, J. Hu, K. Wong, C. Fang, C. Wang, X. Han, Q. Shao, T. Taniguchi, K. Watanabe, J. Zang, Z. Mao, X. Zhang, K. L. Wang, Néel-type skyrmion in WTe2/Fe3GeTe2 van der Waals heterostructure. arXiv:1907.11349 [cond-mat.mtrl-sci] (26 July 2019).

32. H. Wang, C. Wang, Y. Zhu, Z.-A. Li, H. Zhang, H. Tian, Y. Shi, H. Yang, J. Li, Direct observations of chiral spin textures in van der Waals magnet Fe3GeTe2 nanolayers. arXiv:1907.08382 [cond-mat.mtrl-sci] (19 July 2019).

33. P. J. H. Bloemen, W. J. M. de Jonge, Determination of the ferromagnetic coupling across Pd by magneto-atomic engineering. *J. Appl. Phys.* **73**, 4522 (1993).

34. N. Nakajima, T. Koide, T. Shidara, H. Miyauchi, A. Fujimori, K. Iio, T. Katayama, M. Nývlt, Y. Suzuki, Perpendicular magnetic anisotropy caused by interfacial hybridization via enhanced orbital moment in Co/Pt multilayers: Magnetic circular x-ray dichroism study. *Phys. Rev. Lett.* **81**, 5229–5232 (1998).

35. B. Tudu, K. Tian, A. Tiwari, Effect of composition and thickness on the perpendicular magnetic anisotropy of (Co/Pd) multilayers. *Sensors* **17**, 2743 (2017).

36. W. Jiang, P. Upadhyaya, W. Zhang, G. Yu, M. B. Jungfleisch, F. Y. Fradin, J. E. Pearson, Y. Tserkovnyak, K. L. Wang, O. Heinonen, S. G. E. te Velthuis, A. Hoffmann, Blowing magnetic skyrmion bubbles. *Science* **349**, 283–286 (2015).

37. S. D. Pollard, J. A. Garlow, J. Yu, Z. Wang, Y. Zhu, H. Yang, Observation of stable Néel skyrmions in cobalt/palladium multilayers with Lorentz transmission electron microscopy. *Nat. Commun.* **8**, 14761 (2017).

38. M. J. Benitez, A. Hrabec, A. P. Mihai, T. A. Moore, G. Burnell, D. McGrouther, C. H. Marrows, S. McVitie, Magnetic microscopy and topological stability of homochiral Néel domain walls in a Pt/Co/AlOx trilayer. *Nat. Commun.* **6**, 8957 (2015).

39. C. Ophus, T. Ewalds, Guidelines for quantitative reconstruction of complex exit waves in HRTEM. *Ultramicroscopy* **113**, 88–95 (2012).

Citation: M. Yang, Q. Li, R. V. Chopdekar, R. Dhall, J. Turner, J. D. Carlström, C. Ophus, C. Klewe, P. Shafer, A. T. N'Diaye, J. W. Choi, G. Chen, Y. Z. Wu, C. Hwang, F. Wang, Z. Q. Qiu, Creation of skyrmions in van der Waals ferromagnet Fe3GeTe2 on (Co/Pd)n superlattice. *Sci. Adv.* **6**, eabb5157 (2020).